PHYSICAL REVIEW B **89**, 085418 (2014)

Compositionally modulated ripples during composite film growth: Three-dimensional pattern formation at the nanoscale

Matthias Krause,[1,2,*] Maja Buljan,[3] Arndt Mücklich,[1] Wolfhard Möller,[1] Monika Fritzsche,[1,2] Stefan Facsko,[1] René Heller,[1]
Matthias Zschornak,[1] Sebastian Wintz,[1,2] Jose Luis Endrino,[4] Carsten Baehtz,[1,5] Artem Shalimov,[1,5]
Sibylle Gemming,[1,6] and Gintautas Abrasonis[1]
[1]*Helmholtz-Zentrum Dresden-Rossendorf, P.O. Box 510119, D-01314 Dresden, Germany*
[2]*Technische Universität Dresden, D-01062 Dresden, Germany*
[3]*Rudjer Bošković Institute, Bijenička cesta 54, 10000 Zagreb, Croatia*
[4]*Abengoa Research S.L., Abengoa, Campus Palmas Altas, Calle Energía Solar 1, Seville 41014, Spain*
[5]*Rossendorf Beamline, European Synchrotron Radiation Facility, F-38043 Grenoble, France*
[6]*Faculty of Science, Technische Universität Chemnitz, D-09107 Chemnitz, Germany*

(Received 1 March 2013; revised manuscript received 18 December 2013; published 21 February 2014)

Three-dimensional, ion-induced nanoscale pattern formation in the growth mode is studied for a bicomponent thin film. C:Ni films were grown by dual ion beam cosputtering applying an assisting oblique-incidence low-energy Ar^+ ion beam. Their microstructure was determined by scanning electron, atomic force, and transmission electron microscopy, as well as by grazing-incidence small-angle x-ray scattering. The role of ion-induced collisional effects was investigated by binary collision computer simulations. The formation of compositionally modulated ripples on the C:Ni film surface is demonstrated. They consist of metal-enriched topographic crests and carbon-enriched valleys. Since the surface is constantly covered by incoming species, this pattern is transferred into the bulk as a periodic array of Ni_3C nanoparticles or of Ni-enriched regions in a carbon matrix. Lateral ripple propagation is shown to be one of the crucial phenomena for the film morphology. The essential experimental features are reproduced by the computer simulations. The results reveal the importance of ion-induced preferential displacements as the driving factor for a surface instability, which gives rise to the observed pattern formation.

DOI: 10.1103/PhysRevB.89.085418 PACS number(s): 81.16.Rf, 68.55.J−, 79.20.Rf, 81.15.Jj

I. INTRODUCTION

Self-organization at the nanoscale offers a potential bottom-up route to control the microstructure of materials in one (1D), two (2D), and three dimensions (3D). It occurs at nonequilibrium conditions and requires an external energy source, which is not the primary ordering source but a constraint [1]. Surface instabilities far from the thermodynamic equilibrium are a particular case of self-organization. They can occur during thin-film growth and may induce surface roughness nanopattern formation [2]. For multicomponent materials, instability-induced surface roughness can couple to the local surface composition [3–14]. Such a coupling produces a compositional nanopattern on the film surface. Provided that the film is constantly buried by incoming species, which are again driven to pattern formation due to the instability, such a situation can result in the formation of 3D-ordered heterogeneous structures. Examples of such structures are nanocomposites (NCs) [15] or encapsulated arrays of nanoparticles (NPs), where a solid matrix material "locks" in space the 3D array of NPs which is otherwise mechanically unstable [16]. The scale of the pattern depends on kinetic and thermodynamic factors such as adatom diffusivity, substrate mismatch stresses, compositional stresses, and phase stability [2]. NC material properties at the macroscale are strongly influenced by the microstructure and morphology at the nanoscale [15]. Therefore, any opportunities to influence and control surface instabilities are not only of academic interest, but also provide powerful means to grow functional heterogeneous nanostructures.

Assisting ion-irradiation during the growth is widely used to influence the microstructure of thin films [17]. It is of particular significance that ions can deliver the energy of ∼1–30 eV per deposited material atom via atomic collisions [18]. This is much larger than the energy provided by other material-specific processes such as phase transformations, interface energy minimization, and recrystallization, which are of the order of ∼1 eV or below [18]. Therefore, ion-induced processes can energetically compete with any material-specific process. In addition, ion irradiation imposes a certain directionality due to momentum transfer [18], which is manifested in microstructural features such as crystallographic [19] or morphological orientation [20].

Ion energy, flux, and incidence angle can often be controlled independently [17,21–23]. This provides easily externally controllable means to tune the "strength" of ion-induced processes in relation to those, which are specific for the thin film/substrate material system. All in all, ion irradiation can create unique processing conditions, which cannot be achieved by any other means.

It has been well established that ion irradiation in the erosion mode induces surface instabilities, which lead to surface pattern formation [24,25]. Moreover, for multicomponent materials these surface roughness patterns can couple to the local composition, resulting in the formation of compositionally modulated surface patterns [26–29]. A recent theoretical study employing linear instability analysis has predicted that ion-induced surface nanopattern formation can occur not only in the erosion but also in the growth mode [30]. Even for thermodynamically stable alloys, phase separation on the growing

---

[*] matthias.krause@hzdr.de

surface can occur, which is driven by ion irradiation [30]. Such phase separation is due to different ballistic properties of the alloy constituents. These compositional modulations can couple to surface roughness features in different ways and induce surface instabilities of different stationary or oscillating types [30].

This work is an experimental demonstration of this paradigm [30]. Three-dimensionally ordered nanocomposites are grown via ion-induced two-dimensional surface nanopattern formation during bicomponent film growth. We show that surface ripples form during oblique-incidence low-energy ion beam assisted deposition of C:Ni films. These surface ripples are compositionally modulated comprising Ni-rich crests and carbon-rich valleys. The film cross sections show a periodic distribution of Ni-rich nanoparticles or of Ni-enriched regions in a carbon matrix, which is a manifestation of the transfer of the surface nanopattern into the bulk. The approach shows potential for the growth of functional NCs or NP arrays with tunable properties.

II. METHODS

A. Film growth and characterization

The C:Ni NC films were grown by dual ion beam sputtering. The base pressure in the high-vacuum chamber was $\sim 1.5 \times 10^{-5}$ Pa. The carbon/nickel vapor was produced by ion beam cosputtering of a 6 inch (15.24 cm) graphite target covered by a 1.5 mm or a 0.5 mm wide Ni stripe at an off-normal angle of $\sim 22^\circ$ and a distance of ~ 17 cm using the Ar^+ beam of a 3 cm Kaufmann-type ion source (IonTech Inc., Fort Collins, USA). The Ar^+ energy was set to 1 keV, and the ion current was 40 mA. The carbon/nickel vapor was deposited on naturally or thermally oxidized (SiO_2 thickness $\sim 0.5\ \mu$m) Si (100) substrates at $(67 \pm 3)\ ^\circ$C at a working pressure of $\sim 1.2 \times 10^{-2}$ Pa. The growing film was irradiated at an oblique-incidence angle of 58° relative to the surface normal by an assisting Ar^+ ion beam with ion energies in the range of 50–140 eV and the total ion beam current of 9 mA, produced by a 4 cm 3-grid Kaufmann-type ion source ISQ40K-F (Ion-Tech GmbH, Wuestenbrand, Germany). This corresponds to estimated nominal ion to atom ratios of ~ 50 [20]. No neutralization of the assisting ion beam was used. Due to space charge effects, for such low ion energies the ion flux arriving at the growing film surface can be significantly smaller than that estimated from the beam diameter and total ion beam current. Therefore, a higher ion energy might also cause an increase in the ion flux at the growing film surface for a constant total beam current.

The atomic film composition and the areal density of the C:Ni NC films were determined by Rutherford backscattering spectrometry and nuclear reaction analysis. The surface morphology of the C:Ni NC films was ascertained by scanning electron microscopy (SEM, Zeiss NVision 40 cross beam), and atomic force microscopy operated in contact mode with a conductive tip in the topographic and conductive mode (AFM, cAFM, Omicron). Cross-sectional transmission electron microscopy [XTEM, Titan 80-300 (FEI)] was used to determine the local microstructure of the C:Ni NC films. The electron microscope was operated at an accelerating voltage of 300 kV. It is equipped with a field emission gun, a SuperTWIN-α lens, and an image corrector providing point resolution of 0.10 nm. The preparation steps for the sample cross sections followed the conventional procedure described by Bravman and Sinclair [31].

Throughout the paper the surface is assigned as the xy plane, with the surface-projected ion beam direction corresponding to the y axis. The direction perpendicular to the surface corresponds to the z axis.

For global microstructure analysis (about 1 mm^2 spot size) 2D grazing-incidence small-angle x-ray scattering (GISAXS; Pilatus 100k detector, wavelength $\lambda = 0.689$ Å, incidence angle $\alpha_i = 0.125^\circ$) at the Rossendorf Beamline ROBL BM 20, ESRF, Grenoble, France, was applied. The probing x-ray beam was either set to lie in the xz or in the yz plane. The detector was at the distance of 343 cm from the sample. Such geometry provided information in the q range of $q =\sim 0.0\ \mathrm{nm}^{-1}$ to $q =\sim 1.0\ \mathrm{nm}^{-1}$. 2D GISAXS images represent essentially the Fourier transformation of the density contrast autocorrelation function [32]. Taking into account that the incidence and scattering angles are small, the horizontal and vertical components of the scattering vector $\mathbf{q}(q_y,q_z)$ are expressed as

$$\mathbf{q} = \frac{2\pi}{\lambda}[\cos(\alpha_{sc})\sin(2\theta_{sc}),\sin(\alpha_i) + \sin(\alpha_{sc})], \qquad (1)$$

where α_{sc} and θ_{sc} are out-of-plane and in-plane x-ray scattering angles, respectively.

B. Binary-collision computer simulation

In order to investigate the role of collisional effects in the formation of the observed structures, the recently developed computer simulation program TRI3DYN has been applied (details of the code will be published elsewhere). Briefly, TRI3DYN represents an extension of the one-dimensional dynamic binary-collision simulation TRIDYN [33–35], which is based on an early sputtering version [36] of the widely used TRIM [37,38] code. TRI3DYN allows to treat multicomponent nanosystems of arbitrary shape under multispecies atomic irradiation, with the option of periodic boundary conditions in lateral directions. The computational volume is configured from fixed 3D cuboid voxels of equal size. Appropriate algorithms have been implemented to treat the transition of projectiles and recoils through the surface. Tracing of sputtered atoms in vacuum voxels allows the simulation of redeposition. Correspondingly, backreflected projectiles may be allowed to repeatedly interact with the surface.

The atomic transport during the collision cascade associated with each impinging atom results in voxels with added or removed atoms (“interstitials” or “vacancies,” respectively), and thereby, in general, in a deviation from the nominal atomic density, which depends on the local composition. Subsequently, such voxels are relaxed to nominal density first by interaction with suitable neighbor voxels or voxels at the surface. Remaining excess or shortfall densities are removed by stepwise material transport between the corresponding voxels or to the surface. During the transport, the composition of the traversed voxels is individually equilibrated to limit the artificial broadening of the 3D compositional distribution.

In a final relaxation step, surface voxels with excess density are allowed to deliver excess material to nearby vacuum voxels, thus creating new surface voxels. Finally, a local surface smoothing procedure is applied by combining nearby density-shortfall surface voxels. Thus, the relaxed system results as an ensemble of vacuum voxels, bulk voxels at nominal density, and surface voxels which may exhibit either nominal density or a density shortfall.

In this way, TRI3DYN allows to simulate the dynamic development of the shape and the composition of nanostructures under a flux of energetic and/or thermal particles. In particular, the surface smoothing algorithm can be regarded as a mechanism of surface atomic transport which is a prerequisite in the description of ion-induced pattern formation at surfaces (see, e.g., Refs. [39,40]).

III. EXPERIMENTAL RESULTS

The C:Ni NC films grown with assisting Ar^+ ion energies from 110 eV to 130 eV consist of Ni-rich nanoparticles (NPs) embedded in an amorphous carbon (a-C) matrix (Fig. 1). Besides a predominantly amorphous phase structure, some distorted crystal planes can be identified in the Ni-rich regions of the TEM images (Fig. 1). Their interplanar distance is of the order of 0.2 nm, which could correspond to the (111) crystal plane distance of fcc Ni, the (101) distance of hexagonal Ni, or the (113) interplanar distance of rhombohedral Ni_3C [41]. Since previous studies of C:Ni NC thin films showed the formation of the cubic Ni phase only at temperatures of 400 °C or higher [42,43], its formation in the present study is excluded. Whether hexagonal Ni or rhombohedral Ni_3C is formed can only be decided by extended x-ray absorption fine structure (EXAFS) investigations. A combined EXAFS and magnetic response study of C:Ni (∼30 at. %) NC films grown without ion assistance revealed the formation of an amorphous Ni carbide phase in the temperature range from room temperature up to 200 °C [43]. Based on the present and the cited results, the phase structure of the Ni-rich phase in this study is assigned to Ni_3C in a predominantly amorphous state.

Depending on the ion energy, two different microstructures are observed (Fig. 1). For the ion energy of ∼110 eV the NPs have a columnar shape [Fig. 1(a)]. The columns are tilted towards the incoming ions ($-y$ direction) by an angle of $(13 \pm 5)^\circ$ relative to the surface normal. Irradiation with Ar^+ ions of ∼130 eV energy induces the formation of tilted, regularly ordered Ni_3C NP chains [Fig. 1(c)]. The tilt of the chains relative to the surface normal occurs in the surface-projected ion-beam direction ($+y$ direction); i.e., the inclination direction changes with the ion energy. Note that an undulated NiSi interlayer of ∼2 to 3 nm thickness is formed between the Si (100) substrate and the C:Ni NC film [Figs. 1(b) and 1(c)] with a carbon-rich zone on its top. The irradiation with ions of ∼120 eV energy results in an intermediate microstructure without nanocolumns, but with a few regular Ni_3C NP chains. The morphological transition from tilted columns to self-organized NP chains is accompanied by a lowered film growth rate and by the decrease of the Ni concentration (from ∼12 at. % for 110 eV to ∼8 at. % for ∼130 eV). The deposition and erosion rates for nickel and

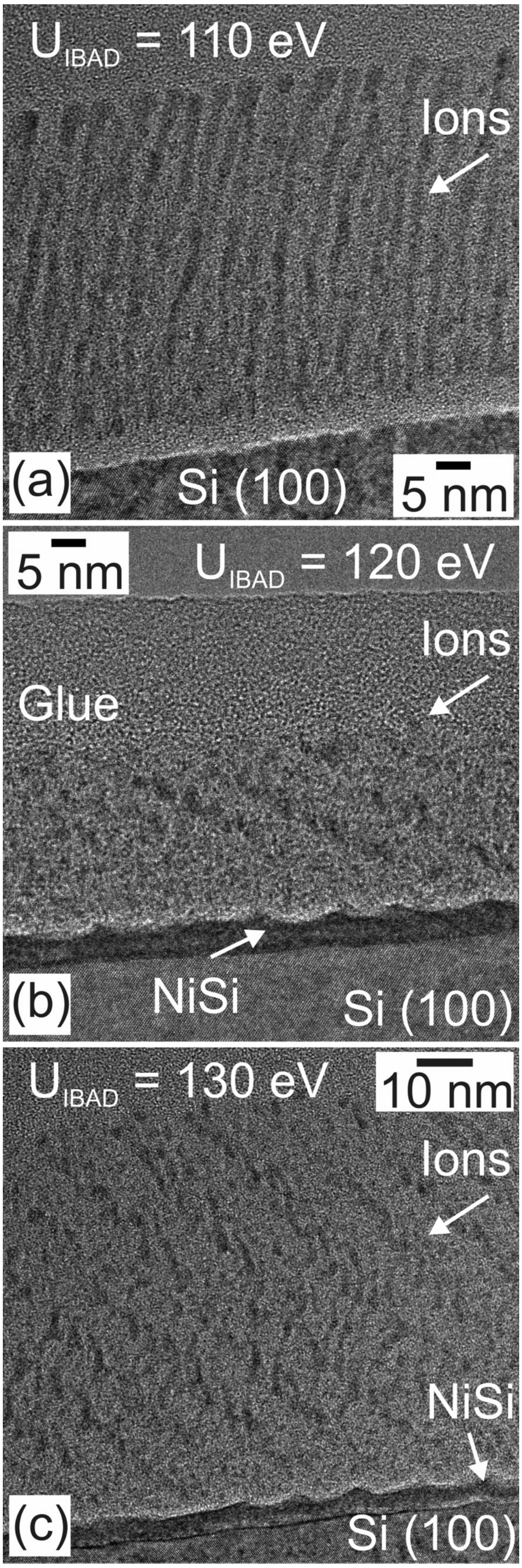

FIG. 1. XTEM images of C:Ni NC thin films deposited on silicon with an assisting Ar^+ beam of (a) 110 eV, (b) 120 eV, and (c) 130 eV ion energy. The TEM cross sections are oriented parallel to the plane of ion incidence (yz plane). The deposition time was 1 h for (a) and (b) and 2 h for (c).

carbon are estimated from the areal densities. The deposition rate of 5.8×10^{17} cm^{-2} h^{-1} was measured without assisting ion irradiation in the same experimental series. The total erosion rates (C + Ni) are roughly given by the difference of deposition rate and measured growth rates. Their values are 4.5×10^{16} cm^{-2} h^{-1} (~8%) and 2.05×10^{17} cm^{-2} h^{-1} (~35%) for C:Ni NC films grown with assisting Ar$^+$ ion irradiation of 110 eV and 130 eV ion energy, respectively. For the C:Ni NC films grown with 130 eV Ar$^+$ ion assistance a significant preferential sputtering of Ni was observed, since the ratios of the erosion and the deposition rates are 0.574 for Ni and 0.323 for carbon. The irradiation of the growing film with Ar$^+$ ions of ~140 eV energy results in its complete resputtering (not shown). The tilted columnar microstructure corresponds to that described and discussed in Ref. [20]. In the following part of the paper we focus on the characterization and discussion of the 3D patterned NP microstructure.

In order to suppress the ion-induced silicide layer formation and to reveal the self-organization dynamics, a C:Ni film was grown with ~130 eV Ar$^+$ ion assistance on a thermally oxidized Si substrate using otherwise identical experimental conditions as above. The surface of the film shows roughness undulations with a period of ~11 nm (Fig. 2). The wave vector of these surface ripples is oriented parallel to the surface-projected ion direction (y). The average crest-to-valley height difference is (1.3 ± 0.8) nm. Conductive AFM measurements gave a 20 times higher current for the NP chains aligned along the ripple crests than for the valley regions [Fig. 2(c)]. The higher currents at the crests are attributed to areas with higher conductivity, while less conductive areas are located in the valleys. Based on the phase structure of the films, the more conductive surface crests are assigned to Ni_3C NPs. Correspondingly, a-C is accumulated in the topographic valleys of the film surface. The different currents reflect the different electric conductivities of Ni_3C and a-C films, which are of the order of $>10^3$ to $\sim 10^5$ ohm^{-1} cm^{-1} and 10^{-2} ohm^{-1} cm^{-1}, respectively [44–46]. A superposition of the cAFM currents with the corresponding AFM topography reveals that the conductivity maxima are located on the crest's backside; i.e., they are slightly y-shifted compared to the surface maxima [Fig. 2(d)].

The ordered Ni_3C NP chains are tilted by ~55° relative to the surface normal [Fig. 2(e)]. The bulk microstructure of the 3D patterned C:Ni NC thin film is characterized by (i) a mean NP diameter of 1.5 ± 0.4 nm, (ii) a mean NP length of 3 ± 1 nm, (iii) a mean intrachain NP distance of 4.3 ± 0.4 nm, and (iv) a mean interchain distance of 6.4 ± 0.6 nm (see Table I). The volume and surface periods are related by the cosine of the NP chain tilt angle . The existence of two well-defined interparticle correlations is revealed by the fast Fourier transformation (FFT) of the XTEM image [inset in Fig. 2(e)]. It shows two sets of spots: (i) two sharp elongated spots close to the center, which are tilted in the direction perpendicular to the NP chains, as well as (ii) two broad spots ~2.3 times farther apart than the first set, which are oriented almost parallel to the film surface. The first set is attributed to the interchain correlation. The sharpness of the spots hints towards a narrow distribution of the involved wavelengths, i.e., a high order of the pattern. The second set is attributed to the inter-particle correlation in the chains. Its significantly broader intensity distribution indicates a much weaker interparticle distance correlation within the chains than between the NP chains. Two growth regimes—"incubation" and "patterning"—can be identified in Fig. 2(e). The ~10 nm thick "incubation" region consists of quasispherical metallic nanoparticles in the carbon matrix with no well-defined interparticle distance. The "patterning" regime is sustained for the rest of the film.

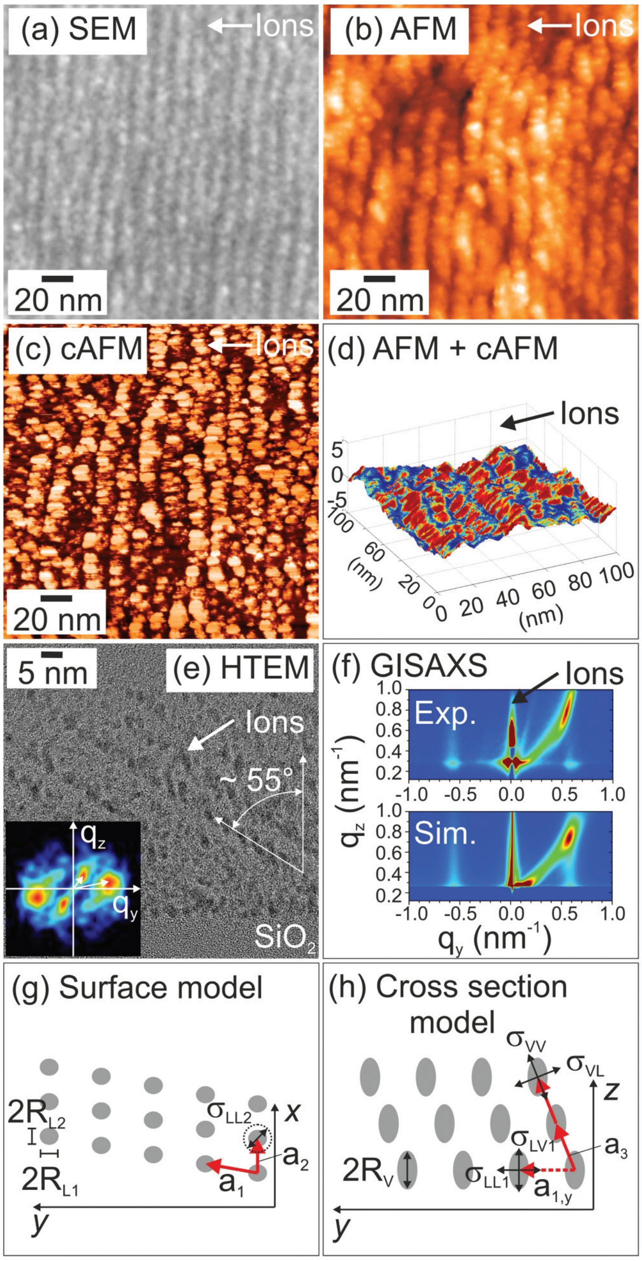

FIG. 2. (Color) Microstructure of the C:Ni NC (~8 at. % Ni) film grown on thermally oxidized Si with an assisting Ar$^+$ beam of 130 eV ion energy. (a) SEM image; (b) AFM image; (c) cAFM image of the same region as (b); (d) 3D overlay of AFM and cAFM image (red: highly conductive regions, blue: less conductive regions); (e) TEM image with its FFT as inset; (f) experimental and simulated GISAXS pattern; (g) and (h) scheme of the paracrystal model used for the GISAXS simulation, showing (g) the plane parallel to the surface and (h) the cross section.

A detailed analysis of the arrangement and the size properties of NPs has been carried out by GISAXS. The GISAXS

TABLE I. Experimental structure parameters in comparison to the NP lattice parameters obtained by the numerical analysis of the GISAXS intensity distribution. The basis vectors of the NP lattice are $\mathbf{a_1} = (1.9, 10.6, 0.0)$, $\mathbf{a_2} = (3.8, 0.0, 0.0)$, and $\mathbf{a_3} = (0.0, 3.2, 2.4)$. The disorder parameters are $\sigma_{LL1(2)}$, $\sigma_{LV1(2)}$, σ_{VL}, and σ_{VV}. $2R_{L1}$ and $2R_{L2}$ correspond to the NP diameters parallel to the film surface, whereas $2R_V$ denotes the NP diameter perpendicular to the film surface.

Parameter	TEM	GISAXS
NP diameter in y direction ($2R_{L1}$) (nm)	1.5±0.4	1.5±0.4
NP diameter in x direction ($2R_{L2}$) (nm)		1.7±0.4
NP length ($2R_V$) (nm)	3±1	3.1±0.5
NP-NP distance in x direction (L_x) (nm)	3.8±0.9	3.8±0.4
NP-NP distance in y direction (L_y) (nm)	10±2	10.6±0.6
Intrachain NP-NP distance (nm)	4.3±0.4	4.3±0.9
Chain tilt angle (deg)	55±1	53.4±0.8
Interchain distance (nm)	6.4±0.6	6.4±0.3
$\sigma_{LL1}/\lvert a_1\rvert$		0.09±0.02
$\sigma_{LV1}/\lvert a_1\rvert$		0.03±0.01
$\sigma_{LL2}/\lvert a_2\rvert$		0.26±0.04
$\sigma_{LV2}/\lvert a_2\rvert$		0.08±0.04
$\sigma_{VL}/\lvert a_3\rvert$		0.25±0.04
$\sigma_{VV}/\lvert a_3\rvert$		0.09±0.02

map, measured with the probing x-ray beam set to lie in the xz plane [see Fig. 2(f)], shows an anisotropic intensity distribution with a sharp tilted intensity streak peaking at $q_y =\sim 0.55\ \mathrm{nm}^{-1}$ and $q_z =\sim 0.79\ \mathrm{nm}^{-1}$. This intensity streak is attributed to strong interchain correlations. Two additional vertical intensity stripes are observed at $q_y = \pm \sim 0.57\ \mathrm{nm}^{-1}$, which might be partially occurring due to the rippled surface of the film [47]. The GISAXS map measured with the probing x-ray beam set to lie in the yz plane (not shown) shows only two symmetric lateral lobes reflecting considerably weaker correlations in the x direction, i.e., parallel to the ripples [see, for example, Fig. 2(c)].

A modified paracrystal model of the NP arrangement (described in detail in Ref. [48]) has been applied for the numerical analysis of the GISAXS pattern. An arrangement of NPs in a 3D NP lattice characterized by the basis vectors $\mathbf{a_1}$, $\mathbf{a_2}$, and $\mathbf{a_3}$ is assumed [Figs. 2(g) and 2(h)]. The deviations of the NP positions from the ordering in an ideal lattice are described by six disorder parameters σ ($\sigma_{LL1(2)}$, $\sigma_{LV1(2)}$, σ_{VL}, σ_{VV}), two for each basis vector ($\mathbf{a_1}$–$\mathbf{a_3}$). They describe disorder in the short-range ordering model, defined in Ref. [48]. The parameters $\sigma_{LL1(2)}$ describe disorder related to the basis vectors a_1 and a_2 in the plane parallel to the surface, while $\sigma_{LV1(2)}$ are related to their disorder in the vertical direction. The parameters σ_{VL} and σ_{VV} describe disorder related to the basis vector a_3 in directions parallel and perpendicular to it, respectively. A schematic illustration of the effect of disorder parameters is indicated in Figs. 2(g) and 2(h). The theory explaining the details of disorder in the system is given in Ref. [48]. The NP shape is assumed to be ellipsoidal with radii R_{L1} and R_{L2} in direction parallel to the film surface and R_V perpendicular to it [see Figs. 2(g) and 2(h)]. Note that the surface ripples are not included in the paracrystal model. The parameters of the paracrystal model were obtained by fitting the experimental GISAXS pattern (Table I).

The simulated GISAXS pattern reproduces the major features of the experimental one [Fig. 2(f)]. Both types of stripes (vertical and inclined) are the consequence of the existence of a 3D lattice of NPs. The contribution of the ripples is very small due to the much smaller electron contrast between the ripples and vacuum than between Ni_3C NPs and surrounding a-C matrix. Additionally, the number of NPs that contribute to the scattering is significantly larger than the number of ripples, so the ripples' contribution can be neglected in the fitting process. The results of the GISAXS analysis are in excellent agreement with the results of all the other local structural analysis techniques. The distances between the NPs are found significantly larger (10.6 nm) in the surface-projected ion beam direction (y direction) than in the x direction (3.8 nm). The deviation of the interchain distances within the direction parallel to the substrate σ_{LL1} is less than 10% (direction $\mathbf{a_1}$). The smallest deviation of only 3% (or the highest correlation) is found for the angular deviation between the center-to-center distances of NPs of neighboring chains (the deviation perpendicular to the $\mathbf{a_1}$ direction). Note that the $\mathbf{a_1}$ direction has the strongest overlap with the incident ion direction. The correlation between the particles in the chains (σ_{VL}, direction $\mathbf{a_3}$) as well as along the ripples (σ_{LL2}, direction $\mathbf{a_2}$) is significantly weaker ($\sigma_{VL} \approx \sigma_{LL2} \sim 25\%$).

The periodic surface and bulk pattern is also formed for assisting Ar^+ energies as low as ~50 eV, provided that the Ni content is slightly lower than in the case discussed before, i.e., about 5 at. % nominal (see Fig. 3). The surface period is ~20 nm and thereby almost by a factor of 2 larger than that for C:Ni (~8 at. % Ni) grown with 130 eV Ar^+ ion irradiation. The XTEM image shows periodic contrast modulations. The regions with stronger electron scattering contrast are enriched with Ni. The average distance of the contrast modulations (13 nm) corresponds closely to the product of cosine 40° (tilt angle) and surface period. Along with the periodicities themselves, this relationship is the crucial observation for the context of this work. Though the Ni-enriched regions appear discontinuous, thus indicating the formation of NPs, the very low contrast prevents their unambiguous identification and analysis [Fig. 3(b)]. Therefore, the Ni phase structure remains open in this case. Again the stability of the 3D pattern formation process is demonstrated for the entire film thickness of about ~160 nm (Fig. 3).

IV. TRI3DYN SIMULATIONS

An examplary TRI3DYN simulation shows the formation of periodic topographic surface undulations during the Ar^+ ion assisted growth of C:Ni (15 at. %) films [see Fig. 4(c)]. The period is of the order of ~20 nm, and the crest-to-valley height difference is ~5 nm. The cross section shows that the atomic distribution is not homogeneous but contains areas enriched in Ni [see Figs. 4(a) and 4(b)]. The maximum Ni atomic density variation between metal rich and depleted areas is of the order of 20%–30% relative to the average Ni atomic density. The period of these compositional modulations corresponds to the period of the surface ripples. The Ni-rich areas are tilted in relation to the film surface in the y direction, along the incoming Ar^+ beam. The ratio of sputtered to incoming atoms is ~0.39 for Ni, and ~0.32 for carbon, or in other words, the

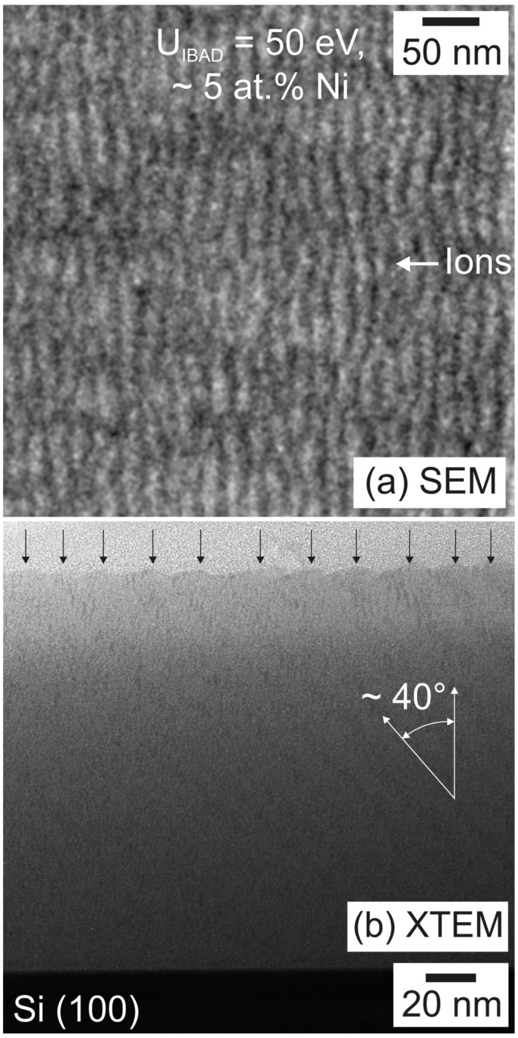

FIG. 3. Microstructure of the C:Ni film (~5 at. % Ni nominal) deposited on thermally oxidized Si with an assisting Ar^+ beam of 50 eV ion energy: (a) SEM image; (b) XTEM image taken with 115 kx magnification. A 300 nm defocused electron beam was applied to highlight the surface crests in the TEM image. The crests are indicated by arrows.

resputtering yield for nickel is by about 22% higher than for carbon. Note that on the very surface Ni-rich areas are on the ripple side facing the ion beam while underneath the surface Ni-rich areas are on the ion beam averted side of the ripples. The growth kinetics shows a transition from the erosion mode at the initial stages of the film growth to the growth mode at the fluence of $\sim 7.5 \times 10^{16}$ cm^{-2} [Fig. 4(d)]. This correlates with the observation of the undulated C:Ni/Si interface indicating that the deposition (growth)/erosion balance depends not only on the ion energy, incidence angle, and ion-to-atom ratio but also on the surface morphology. The system self-adapts to the morphology which minimizes erosion due to sputtering. Also note a transition layer at the interface which is depleted of nickel. Additional simulations indicate (not shown) that the increase in ion-to-atom ratio increases the ripple period but also decreases significantly the growth rate of the film.

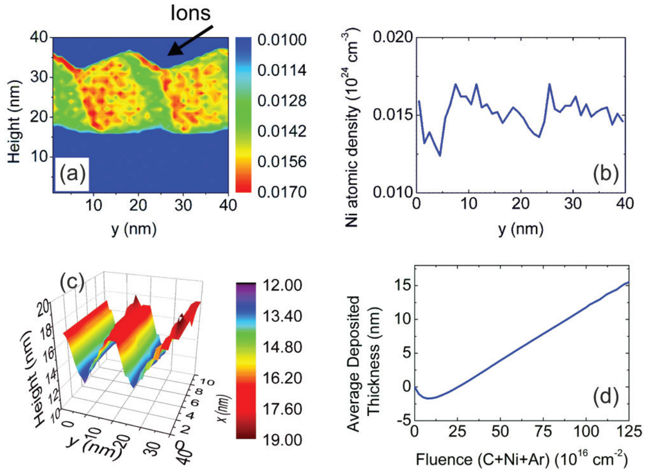

FIG. 4. (Color) TRI3DYN simulation of the growth of a C:Ni film on a Si substrate: (a) cross section of the simulated film area. The color contrast represents the Ni atomic density in units of 10^{24} cm^{-3} averaged in the x direction (i.e., over all voxels with the same y and z coordinates); (b) Ni atomic density variation at the height of 27 nm of the panel (a); (c) surface topography of the film; (d) deposited thickness as a function of total (i.e., C+Ni+Ar) fluence. The incident Ni to C flux ratio is 0.176, and the Ar^+ ion-to-atom ratio is 3. The Ar^+ ion energy is 130 eV at an incidence angle of 60°; the C and Ni atom energy is 0 eV at an incidence angle of 0°. The simulated volume contains $40 \times 40 \times 10$ voxels of the volume of $1 \times 1 \times 1$ nm^3.

V. DISCUSSION

The results above demonstrate that at certain growth conditions of C:Ni NC films the assisting ion irradiation induces regular topographical and compositional surface structures. Such regular surface patterns are neither formed during the growth of dispersed metal NP or nanocolumns in a carbon matrix by ion beam sputter codeposition of transition metals and carbon [49], nor during dual ion beam cosputter growth of tilted nanocolumns [20], nor during the formation of self-organized multilayers (tilted or “lying”) using filtered-cathodic vacuum arc deposition [50–52]. Hence the surface pattern formation observed in this work must be attributed to a different structure-determining mechanism than in the mentioned cases, where repeated nucleation [50,53], thermally or ion-enhanced surface diffusion [20,53], ion-induced surface atomic drift [20], and subplantation [52] were identified as driving mechanisms.

The crucial observation supporting an ion-induced surface instability mechanism is the ratio between the NP-NP distance in the y direction (L_y) and x direction (L_x) of about ~3 (see Fig. 2 and Table I). Note that L_x is close to the NP-NP distance observed in the columnar growth mode [see Fig. 1(a)]. This distance is related to the magnitude of the surface diffusivity [54,55]. If phase separation was the driving mechanism for the pattern formation [28], the characteristic length of such a pattern would scale with the Ni diffusivity and would be of the order of L_x or of the NP-NP distance in the columnar growth mode (~4 nm). Therefore, L_y must be caused by an ion-induced surface instability. Phase separation does not induce but *follows* the ion-induced pattern with nucleation and growth occurring at the Ni-rich regions close to ripple crests.

This observation enables a significant simplification in terms of interpretation from the theoretical point of view. At such low Ni concentrations (∼ 5 to 8 at. %) the phase separation takes place in nucleation and growth mode [53]. An analytical theoretical treatment of phase separation in the nucleation and growth mode during film growth to our knowledge is lacking. The fact that ordering is caused by ion irradiation allows us to use the theoretical treatment for ion-induced instabilities in alloys [30,56,57], while at the same time phase separation processes can be neglected at least for the qualitative understanding. It also justifies the use of binary-collision simulation codes such as TRI3DYN.

The formation of surface ripples can be explained by surface instabilities due to the preferred ion-induced displacement at valleys compared to that at crests [39,40,58]. Note that here the term "displacement" includes both—ion-induced atomic relocations and sputtering [30]. Such ion-induced ripples have been predicted by linear instability theory [30] and have been observed experimentally in a-C films [59].

The topographic pattern couples to the atomic surface composition leading to compositionally modulated surface ripples (see Fig. 2). For the *erosion* mode the coupling between roughness and composition patterns has been predicted by Shenoy and Chason [56]. It necessitates the preferential displacement of one of the components in the erosion [56,57] or growth [30] mode (nickel in the case of this study). If Ni atoms appear at ballistically "unfavorable" sites (valleys in the present case), they are preferentially either resputtered or relocated towards ballistically more "favorable" sites, i.e., towards the crests. In such a manner the crests are enriched with Ni. If the surface diffusivities of the two species are not extremely different, the preferentially displaced element is expected to accumulate at peaks [56]. This is in agreement with the observations of this study in which the preferentially sputtered element Ni shows the tendency to accumulate close to the ripple crests (see Fig. 2).

The surface nanopatterns obtained in this work indicate a relatively narrow instability wavelength band (the ratio σ_{LL1}/a_1 is 9%; see Table I). This corresponds to an instability of type I [60]. Following the linear instability theory of the ion-assisted growth of alloy films [30], such instability type can only occur in the presence of preferential displacement and preferential diffusivity. In addition, the preferentially displaced element must also have higher thermal or ballistic diffusivity. This is in agreement with the experimental situation of this study where Ni is preferentially displaced as well as that it exhibits a larger surface diffusivity [20]. Alternatively, the high degree of ordering can be attributed to the selectivity of one dominating wavelength in the nonlinear mode. Note that in this context the nonlinear regime would have been reached very quickly (only a couple of nanometers of the intermediate layer) and would stay in the steady state for the rest of the film thickness.

During film growth the surface is constantly covered by a homogeneous mixture of carbon and nickel depositing from the vapour phase and the surface pattern is transferred into the bulk of the film. Simultaneously the surface is again patterned due to the ion-induced instability. As the bulk atomic mobility is negligible at the deposition temperatures of this study [20,50], the pattern gets 'frozen' within the film.[54] In such a way, the ion-induced 2D surface nanopatterning results in the 3D nanopatterning of a growing film.

The observed NP chain tilt is attributed to the ripple propagation along the irradiated surface [61,62]. The tilt angle results from the surface movement in the vertical direction due to the growth and the lateral surface ripple propagation (0.008 and 0.014 nm s^{-1} at 50 eV and 130 eV, respectively, as determined from the net growth rates and the observed tilt angle). The observed phase shift between the composition and surface roughness modulations [Fig. 2(d)] goes beyond the work of Shenoy and Chason, who predicted a phase shift of either 0° or 180° between roughness and composition fields [56]. Their theory did not include the first-order terms responsible for ripple movement along the surface. This indicates that the ripple velocity not only induces the tilt of the nanopattern, but probably also the observed phase shift. Note that the repeated nucleation occurs in a relatively regular fashion once the nickel nanoparticles get buried by laterally moving carbon-rich zones. This introduces the second scale in the nanopattern, i.e. that of the lateral interparticle distance within the chains [see Fig. 2(e)]. Also note that such lateral movements themselves can produce surface instabilities which couple surface roughness and local composition [63].

The TRI3DYN simulation results agree qualitatively with the experimental observations of this study. This agreement includes the formation of surface ripples, the compositional modulation of the ripples, the correspondence of the compositional periodicity and that of the surface undulations, the tilt of the Ni-enriched areas in the bulk, the preferential resputtering of Ni in comparison to C, as well as the formation of a Ni-depleted interface layer [compare Figs. 1(c) and 4(a)]. The ratio of sputtered to incoming atoms is quantitatively reproduced for carbon (experiment: 0.32; simulation: 0.32), and qualitatively reproduced for nickel (experiment: 0.57; simulation: 0.39). The degree of agreement is surprising taking into account that TRI3DYN simulations do not consider any thermal diffusion or other thermodynamic effects such as the nucleation of new phases. This agreement emphasizes the crucial importance of ballistic effects for the nanopattern formation, especially the role of ballistic relocations. One can expect that surface smoothening due to other mechanisms such as curvature gradient induced thermal diffusion [39] would produce lower crest-to-valley values (surface diffusion effect). One can also expect that in the Ni-enriched areas nucleation and growth of nickel carbide NPs will take place (thermodynamic effect) thus enhancing the material composition contrast. When not neglected, both effects are expected to bring the simulation approach closer to the experimental observations. However, the combined influence of such effects on the final microstructure requires more sophisticated simulation approaches such as the inclusion of thermal and thermodynamic effects directly into the binary-collision code or the combination of the binary-collision approach with kinetic Monte Carlo simulations [64]. For a quantitative comparison between the experimental results and the simulations, one should note that the surface instability is very sensitive to the growth parameters as demonstrated in this study (see Fig. 1). In addition, a precise experimental knowledge of the ion-to-atom ratio is required. This will be addressed in future studies.

VI. CONCLUSIONS

The formation of surface nanopatterns during the growth of C:Ni films by means of dual ion beam cosputtering and binary collision simulations has been studied. The patterning regime is reached by an increase of the ion energy (ion flux) or/and a decrease of the Ni content compared to the previously described tilted nanocolumn regime [20]. The nanopatterning mode is characterized by the formation of regular 2D surface nanopatterns coupling to the surface roughness and local composition modulations. The film growth in this mode results in the formation of a 3D nanopattern consisting of ordered arrays of metal carbide NPs embedded in a carbon matrix. The nanopatterns have several characteristic length scales such as NP diameter and height and interparticle distance within and between the chains. The nanopatterning mode is sustained after a short "incubation" time over the whole film thickness. The experiments and binary collision simulations strongly indicate the dominance of Ar^+ ion-induced ballistic effects in relation to thermodynamic effects to cause the surface instabilities. The formation of such a pattern is consistent with the ion-induced surface instability theories based on the differences in ballistic properties of film components [30,56,57]. It has been also demonstrated that the ripple movement on the surface is an important structure forming factor causing the tilt of the nanopattern relative to the film surface and influencing the repeated nucleation of the metal carbide NPs.

Ion-induced surface nanopatterns have been observed in different materials and material classes such as metals, semiconductors, or dielectrics [24]. The pattern formation is driven by ballistic effects of ion irradiation. The key factor is the reduced bulk mobility once the pattern is buried by incoming species. It prevents any thermodynamically driven mass redistribution in the bulk. The dependence on ion energy, ion-to-atom ratio, surface composition, and nucleation and growth towards spinodal modes or non-phase-separating alloy systems should be explored to demonstrate the extent of the applicability of the ballistic effects outlined above. Such investigations would allow an estimation of the extent to which the results reported in this study hold potential to become a general approach for the growth of functional NCs and encapsulated NP arrays with tunable properties. For example, it can be used to tune the refractive index in combination with laser irradiation stability of phase shift in optical nanocomposites [65,66]. By employing plasmonic metals in dielectric or semiconducting matrices, the approach can be used to influence the lateral plasmon enhanced electric field for sensing [67] or photocatalytic [68] applications. Similarly, such nanostructures are expected to effect electron and phonon transport, and are thus relevant for thermoelectric energy conversion [69]. Ordered embedded metal nanostructures are promising candidates as metamaterials [70–72]. Our study shows the potential to sculpt simultaneously at several scales: NP size, shape, interparticle, and interchain scales. This is of relevance for the next generation of metamaterials [72]. The possibility to change the ion direction during the growth by sample in-plane rotation or tilting can be used to grow more complex tilted superstructures such as chevrons or helices [20]. Note that the azimuthal sample rotation might not even be needed as the tilting above some critical angle produces ripples, and thus nanopatterns, in a perpendicular direction [24].

ACKNOWLEDGMENTS

This work was funded by the EU, "European Regional Development Fund," Project ECEMP-D1 (No. 13857/2379), "Nanoskalige Funktionsschichten auf Kohlenstoffbasis," and LEI 100114022 "C-basierte Funktionsschichten für tribologische Anwendungen." M.B. acknowledges the Croatian Ministry of Science Education and Sports (Project No. 098-0982886-2859). We thank the ESRF, Grenoble, France, for providing synchrotron radiation facilities. The technical assistance of Dr. F. Munnik, Dr. A. Kolitsch, J. Wagner, M. Steinert, C. Frenzel, A. Kunz, M. Missbach, and A. Scholz (all HZDR) is gratefully acknowledged. Dr. J. Grenzer is acknowledged for helpful discussions.

---

[1] J. D. Halley and D. A. Winkler, Complexity **14**, 10 (2008).
[2] P. Politi, G. Grenet, A. Marty, A. Ponchet, and J. Villain, Phys. Rep. **324**, 271 (2000).
[3] J. Tersoff, Phys. Rev. Lett. **77**, 2017 (1996).
[4] J. Tersoff, Phys. Rev. B **56**, R4394 (1997).
[5] P. Venezuela and J. Tersoff, Phys. Rev. B **58**, 10871 (1998).
[6] P. Venezuela, J. Tersoff, J. A. Floro, E. Chason, D. M. Follstaedt, F. Liu, and M. G. Lagally, Nature (London) **397**, 678 (1999).
[7] J. E. Guyer and P. W. Voorhees, Phys. Rev. Lett. **74**, 4031 (1995).
[8] J. E. Guyer and P. W. Voorhees, Phys. Rev. B **54**, 11710 (1996).
[9] J. E. Guyer and P. W. Voorhees, J. Cryst. Growth **187**, 150 (1998).
[10] B. J. Spencer, P. W. Voorhees, and J. Tersoff, Phys. Rev. B **64**, 235318 (2001).
[11] F. Leonard and R. C. Desai, Phys. Rev. B **57**, 4805 (1998).
[12] F. Leonard and R. C. Desai, Phys. Rev. B **56**, 4955 (1997).
[13] F. Leonard and R. C. Desai, Phys. Rev. B **55**, 9990 (1997).
[14] F. Leonard, M. Laradji, and R. C. Desai, Phys. Rev. B **55**, 1887 (1997).
[15] P. M. Ajayan, L. S. Schadler, and P. V. Braun, *Nanocomposite Science and Technology* (Wiley-VCH, Weinheim, 2005).
[16] J. C. C. Fan, US Patent No. 4312915 (filed 1982).
[17] F. Smidt, Int. Mater. Rev. **35**, 61 (1990).
[18] J. M. E. Harper and K. P. Rodbell, J. Vac. Sci. Technol. B **15**, 763 (1997).
[19] J. M. E. Harper, in *Artifically Induced Grain Alignment in Thin Films*, edited by V. Matias, R. Huhne, S. H. Moon, and R. Hammond (Materials Research Society, Warrendale, PA, 2009), Vol. 1150 of Materials Research Society Symposium Proceedings, p. 3.
[20] M. Krause, A. Muecklich, T. W. H. Oates, M. Zschornak, S. Wintz, J. L. Endrino, C. Baehtz, A. Shalimov, S. Gemming, and G. Abrasonis, Appl. Phys. Lett. **101**, 053112 (2012).

[21] J. Harper, J. Cuomo, R. Gambino, and H. Kaufman, Nucl. Instrum. Methods Phys. Res., Sect. B **7–8**, 886 (1985).
[22] J. Colligon, J. Vac. Sci. Technol. A **13**, 1649 (1995).
[23] J. Colligon, Philos. Trans. R. Soc. A **362**, 103 (2004).
[24] W. L. Chan and E. Chason, J. Appl. Phys. **101**, 121301 (2007).
[25] D. Cahill, J. Vac. Sci. Technol. A **21**, S110 (2003).
[26] S. Macko, F. Frost, M. Engler, D. Hirsch, T. Hoeche, J. Grenzer, and T. Michely, New. J. Phys. **13**, 073017 (2011).
[27] J. Zhou, S. Facsko, M. Lu, and W. Moeller, J. Appl. Phys. **109**, 104315 (2011).
[28] K. Zhang, M. Broetzmann, and H. Hofsaess, New. J. Phys. **13**, 013033 (2011).
[29] A. Redondo-Cubero, R. Gago, F. J. Palomares, A. Mücklich, M. Vinnichenko, and L. Vázquez, Phys. Rev. B **86**, 085436 (2012).
[30] G. Abrasonis and K. Morawetz, Phys. Rev. B **86**, 085452 (2012).
[31] J. Bravman and R. Sinclair, J. Elect. Mic. Tech. **1**, 53 (1984).
[32] R. Lazzari, *X-Ray and Neutron Reflectivity: Principles and Applications* (Springer, Berlin, 2009), Vol. 770 of Lecture Notes in Physics, Chap. 7.
[33] W. Moller and W. Eckstein, Nucl. Instr. Meth. Phys. Res, Sect. B **2**, 814 (1984).
[34] W. Moller, W. Eckstein, and J. Biersack, Comput. Phys. Commun. **51**, 355 (1988).
[35] W. Möller and M. Posselt, TRIDYN, http://www.hzdr.de/db/Cms?pNid=310&pOid=21578.
[36] J. Biersack and W. Eckstein, Appl. Phys. A **34**, 73 (1984).
[37] J. Biersack and L. Haggmark, Nucl. Instr. Meth. **174**, 257 (1980).
[38] J. Ziegler, Particle Interactions with Matter, http://www.srim.org.
[39] R. Bradley and J. Harper, J. Vac. Sci. Technol. A **6**, 2390 (1988).
[40] C. S. Madi, E. Anzenberg, K. F. Ludwig, Jr., and M. J. Aziz, Phys. Rev. Lett. **106**, 066101 (2011).
[41] Powder diffraction file, International Center for Diffraction Data, card 00-004-0850 for fcc Ni, card 01-089-7129 for hexagonal Ni, card 00-006-0697 for rhombohedral nickel carbide.
[42] G. Abrasonis, M. Krause, A. Mücklich, K. Sedlacková, G. Radnóczi, U. Kreissig, A. Kolitsch, and W. Möller, Carbon **45**, 2995 (2007).
[43] G. Abrasonis, A. Scheinost, S. Zhou, R. Torres, R. Gago, I. Jiménez, K. Küpper, K. Potzger, M. Krause, A. Kolitsch *et al.*, J. Phys. Chem. C **112**, 12628 (2008).
[44] M. Sikkens, Sol. Energy. Mater. **6**, 403 (1982).
[45] R. Koppert, S. Uhlig, H. Schmid-Engel, D. Goettel, A. Probst, G. Schultes, and U. Werner, Diam. Relat. Mater. **25**, 50 (2012).
[46] J. Robertson, Adv. Phys. **35**, 317 (1986).
[47] A. Biermanns, U. Pietsch, J. Grenzer, A. Hanisch, S. Facsko, G. Carbone, and T. H. Metzger, J. Appl. Phys. **104**, 044312 (2008).
[48] M. Buljan, N. Radic, S. Bernstorff, G. Drazic, I. Bogdanovic-Radovic, and V. Holy, Acta Crystallogr. A **68**, 124 (2012).
[49] M. Berndt, M. Krause, G. Abrasonis, A. Muecklich, F. Munnik, A. Kolitsch, and W. Moeller, Plasma Process. Polym. **6**, S902 (2009).
[50] G. Abrasonis, G. J. Kovács, L.Ryves, M. Krause, A. Mücklich, F. Munnik, T. W. H. Oates, M. M. M. Bilek, and W. Möller, J. Appl. Phys. **105**, 083518 (2009).
[51] G. Abrasonis, T. W. H. Oates, G. J. Kovács, J. Grenzer, P. O. A. Persson, K.-H. H. Heinig, A. Martinavičius, N. Jeutter, C. Baehtz, M. Tucker *et al.*, J. Appl. Phys. **108**, 043503 (2010).
[52] G. Abrasonis, G. J. Kovacs, M. D. Tucker, R. Heller, M. Krause, M. C. Guenette, F. Munnik, J. Lehmann, A. Tadich, B. C. C. Cowie *et al*., Appl. Phys. Lett **97**, 163108 (2010).
[53] G. Abrasonis, G. J. Kovács, A. Mücklich, S. Zhou, D. Babonneau, A. Martinavičius, M. Berndt, F. Munnik, M. Vinnichenko, K. H. Heinig *et al*., J. Phys. Chem. C **113**, 8645 (2009).
[54] M. Atzmon, D. A. Kessler, and D. J. Srolovitz, J. Appl. Phys. **72**, 1707 (1992).
[55] N. Yasui, R. Horie, Y. Ohashi, K. Tanji, and T. Den, Adv. Mater. **19**, 2797 (2007).
[56] V. B. Shenoy, W. L. Chan, and E. Chason, Phys. Rev. Lett. **98**, 256101 (2007).
[57] R. M. Bradley and P. D. Shipman, Phys. Rev. Lett. **105**, 145501 (2010).
[58] S. A. Norris, J. Samela, L. Bukonte, M. Backman, F. Djurabekova, K. Nordlund, C. S. Madi, M. P. Brenner, and M. J. Aziz, Nat. Commun. **2**, 276 (2011).
[59] X. Zhu, K. Narumi, Y. Xu, H. Naramoto, and F. Arefi-Khonsari, J. Appl. Phys. **95**, 4105 (2004).
[60] M. Cross and H. Greenside, *Pattern Formation and Dynamics in Nonequilibrium Systems* (Cambridge University Press, Cambridge, 2009).
[61] S. Habenicht, K. P. Lieb, J. Koch, and A. D. Wieck, Phys. Rev. B **65**, 115327 (2002).
[62] P. F. A. Alkemade, Phys. Rev. Lett. **96**, 107602 (2006).
[63] R. M. Bradley, Phys. Rev. B **85**, 115419 (2012).
[64] B. Liedke, Ph.D. thesis, Technische Universität Dresden, 2011.
[65] O. Stenzel, S. Wilbrandt, M. Schuermann, N. Kaiser, H. Ehlers, M. Mende, D. Ristau, S. Bruns, M. Vergoehl, M. Stolze *et al.*, Appl. Optics **50**, C69 (2011).
[66] D. Nguyen, L. A. Emmert, I. V. Cravetchi, M. Mero, W. Rudolph, M. Jupe, M. Lappschies, K. Starke, and D. Ristau, Appl. Phys. Lett. **93**, 261903 (2008).
[67] K. A. Willets and R. P. Van Duyne, Annu. Rev. Phys. Chem **58**, 267 (2007).
[68] S. Linic, P. Christopher, and D. B. Ingram, Nat. Mater. **10**, 911 (2011).
[69] P. Pichanusakorn and P. Bandaru, Mater. Sci. Eng., R **67**, 19 (2010).
[70] J. K. Gansel, M. Thiel, M. S. Rill, M. Decker, K. Bade, V. Saile, G. von Freymann, S. Linden, and M. Wegener, Science **325**, 1513 (2009).
[71] J. Yao, Z. Liu, Y. Liu, Y. Wang, C. Sun, G. Bartal, A. M. Stacy, and X. Zhang, Science **321**, 930 (2008).
[72] L.-P. Carignan, A. Yelon, D. Menard, and C. Caloz, IEEE Trans. Microwave Theory Tech. **59**, 2568 (2011).